



Article

Synthesis and Characterization of $\text{Cu}_2\text{ZnSnSe}_4$ by Non-Vacuum Method for Photovoltaic Applications

Meenakshi Sahu ^{1,2}, Vasudeva Reddy Minnam Reddy ³, Bharati Patro ⁴, Chinho Park ^{2,*}, Woo Kyoung Kim ^{3,*} 
and Pratibha Sharma ^{1,*}

¹ Department of Energy Science and Engineering, Indian Institute of Technology Bombay Powai, Mumbai 400076, India; meenakshisahu.chem@gmail.com

² Korea Institute of Energy Technology (KENTECH), 200 Hyukshin-ro, Naju 58330, Korea

³ School of Chemical Engineering, Yeungnam University, Gyeongsan 38541, Korea; drmvasudr9@gmail.com

⁴ Centre for Research in Nanotechnology and Sciences, Indian Institute of Technology Bombay Powai, Mumbai 400076, India; bharati@iitb.ac.in

* Correspondence: chpark@kentech.ac.kr (C.P.); wkim@ynu.ac.kr (W.K.K.); pratibha_sharma@iitb.ac.in (P.S.)

Abstract: Wet ball milling was used for the synthesis of $\text{Cu}_2\text{ZnSnSe}_4$ (CZTSe) nanoparticles with a kesterite structure. The prepared nanoparticles were used for ink formulation. Surfactants and binders were added to improve the ink stability, prevent agglomeration, and enhance ink adhesion. The films deposited via spin coating were annealed at different temperatures using a rapid thermal processing system in the presence of selenium powder in an inert environment. Analytical techniques, such as X-ray diffraction, Raman spectroscopy, and Fourier-transform infrared spectroscopy, were used to confirm the formation of CZTSe nanoparticles with a single-phase, crystalline kesterite structure. Field-emission scanning electron microscopy and energy-dispersive X-ray spectroscopy were used to study the surface morphology and chemical composition of the thin films before and after annealing, with and without the sodium solution. The optoelectrical properties were investigated using ultraviolet-visible spectroscopy and Hall measurements. All the prepared CZTSe thin films exhibited a p-type nature with an optical bandgap in the range of 0.82–1.02 eV. The open-circuit voltage and fill factor of the CZTSe-based devices increased from 266 to 335 mV and from 37.79% to 44.19%, respectively, indicating a decrease in the number of recombination centers after Na incorporation.

Keywords: $\text{Cu}_2\text{ZnSnSe}_4$; thin film; selenization; photovoltaic devices applications



Citation: Sahu, M.; Minnam Reddy, V.R.; Patro, B.; Park, C.; Kim, W.K.; Sharma, P. Synthesis and Characterization of $\text{Cu}_2\text{ZnSnSe}_4$ by Non-Vacuum Method for Photovoltaic Applications. *Nanomaterials* **2022**, *12*, 1503. <https://doi.org/10.3390/nano12091503>

Academic Editor: Sam Zhang

Received: 24 March 2022

Accepted: 26 April 2022

Published: 28 April 2022

Publisher's Note: MDPI stays neutral with regard to jurisdictional claims in published maps and institutional affiliations.



Copyright: © 2022 by the authors. Licensee MDPI, Basel, Switzerland. This article is an open access article distributed under the terms and conditions of the Creative Commons Attribution (CC BY) license (<https://creativecommons.org/licenses/by/4.0/>).

1. Introduction

The quaternary inorganic semiconductor $\text{Cu}_2\text{ZnSnSe}_4$ (CZTSe) has unique optical and electrical properties. Consequently, they have emerged as ideal solar cell absorbers, replacing Cu(In, Ga)Se₂ (CIGS) and CdTe-based thin-film photovoltaic devices [1,2]. Thus far, CZTSe layers have been deposited using several vacuum- and nonvacuum-based methods. Solar cells built using CZTSe layers fabricated via thermal co-evaporation and direct current (DC) sputtering exhibit power conversion efficiencies (PCE) of 11.6% and 11.95%, respectively [3,4]. Another method to induce CZTSe layer-growth is via the stacking and subsequent selenization of metallic layers. This process has been shown to form materials with a PCE of 9.7% [5]. CZTSe layers grown using solution-based processes have exhibited a PCE of 10.1% [6]. CZTSe thin films developed via the electrochemical route exhibited a PCE of up to 8% [7]. Therefore, CZTSe photovoltaic devices may be capable of attaining high PCE values at a low cost, making CZTSe a promising material for the large-scale production of photovoltaic devices.

Recently, nanoparticle inks prepared using mechanochemical milling have gained considerable attention over other nonvacuum-based processes as a simple, low-cost, and eco-friendly alternative. The nanoparticle-based thin film fabrication process involves

the preparation and subsequent deposition of nanoparticle inks, followed by annealing (selenization) in the presence of Se vapor or H₂Se gas. This procedure is used to prepare a variety of compound materials in numerous applications [8–11]. Shyju et al. (2015) synthesized CZTS and CZTSe thin films in a single-step, ball milling process and studied their physical properties [12]. Tiwari et al. (2017) studied the thermoelectric properties of CZTSe [9]. Malar et al. (2017) explored the effect of milling conditions on the phase purity of CZTSe thin films using Raman spectroscopy [13]. In 2020, Goyal and Malar obtained single-phase CZTSe and investigated its photo-response [14]. Liu et al. (2020) fabricated an SLG/Mo/CZTSe/CdS/i-ZnO/ZnO:Al(AZO)/Al photovoltaic device with an efficiency of 0.18% [15].

Recently, researchers have demonstrated the effective passivation of the grain boundaries in CZTSe absorber layers with the incorporation of alkali metals, particularly sodium, [16–18]. Incorporating alkali metals not only passivates the grain boundaries, surface, and defects but also enhances the crystal quality and carrier concentration of the CZTSe absorber layers [19–22]. Tampo et al. (2020) investigated the impact of Na incorporation in the CZTSe thin film on the morphological and photovoltaic properties as a function of sodium doping [16]. Kim et al. reported the approach for passivation of grain boundaries and defects in the CZTSe samples with and without Na incorporation [17]. Recently, Rehan et al. systematically examined the effects of sodium doping on the performance of CZTSe solar cells thru different sodium incorporation pathways, such as in-situ sodium doping before and after growing thin films [18].

Herein, we present a simple, cost-effective, and environmentally-friendly technique for the preparation of CZTSe nanoparticles and ink materials using a wet mechanochemical process. Thin films were deposited using formulated ink and sodium solutions via the spin-coating method. The post-annealing effects on the spin-coated CZTSe thin films with and without a sodium solution were characterized using X-ray diffraction (XRD), Raman spectroscopy, field-emission scanning electron microscopy (FE-SEM), energy-dispersive X-ray spectroscopy (EDS), ultraviolet-visible (UV-Vis) spectroscopy, and Hall measurements. The photovoltaic properties of the spin-coated CZTSe thin films were analyzed based on their current density—voltage (J-V) characteristics.

2. Materials and Methods

All elemental powders of copper ($\geq 99.5\%$), zinc ($\geq 99.5\%$), tin ($\geq 99.5\%$), and selenium ($\geq 99.99\%$) as well as chemical reagents, such as 1-butanol ($\geq 99.0\%$), methyl ethyl ketone (MEK, ≥ 99.0), Tween-80 (chemically pure grade), and cadmium sulfate ($\geq 99.0\%$), were purchased from Sigma-Aldrich (Saint Louis, MO, USA). Ethanol ($\geq 99.8\%$), sodium borohydride (chemically pure grade), and polyethylene glycol (PEG-400, extra pure grade) were purchased from Fluka (Shin-Dong, Korea), Daejung (Siheung-si, Korea) and Samchun Chemicals (Seoul, Korea), respectively. Thiourea (chemically pure grade) and ammonia solution (chemically pure grade) were obtained from Duksan, Seoul, Korea. All chemicals were used as received without further purification. Commercially available Mo-coated soda-lime glass (SLG) (DKG Co., Daegu, Korea) with a thickness of 0.5 mm and resistivity of $\sim 1.0 \Omega/\text{sq}$ was used for the thin film preparation.

The as-deposited thin films without and with sodium solution were named Se0 and Se0_Na, while the thin films annealed at 500 °C, 520 °C, and 550 °C without and with sodium solution were named Se1, Se2, Se3 and Se1_Na, Se2_Na, Se3_Na, respectively. As fabricated photovoltaic devices using the above annealed thin films were named SC-Se1, SC-Se2, SC-Se3, SC-Se1_Na, SC-Se2_Na, and SC-Se3_Na.

A detailed description of the preparation of CZTSe nanopowders and ink (Figure S1), and fabrication of corresponding thin films and photovoltaic devices was given in our previous report [23] and electronic supplementary information (ESI). Material and device characterization techniques employed in this study were summarized in ESI as well.

3. Result and Discussion

3.1. Zeta Potential and DLS

The dispersion stability profile and hydrodynamic size of the CZTSe ink nanoparticles were determined using zeta potential (dip cell) and dynamic light scattering (DLS) techniques. The results are shown in Figure 1a,b. A mean zeta potential higher than ± 30 mV was observed, thereby confirming the stability of the CZTSe nanocrystals in the prepared ink [24,25]. The negative zeta potential suggests the presence of Se^{2-} ions on the surface of the nanoparticles [26]. The average hydrodynamic size of the CZTSe nanocrystals was 913 nm.

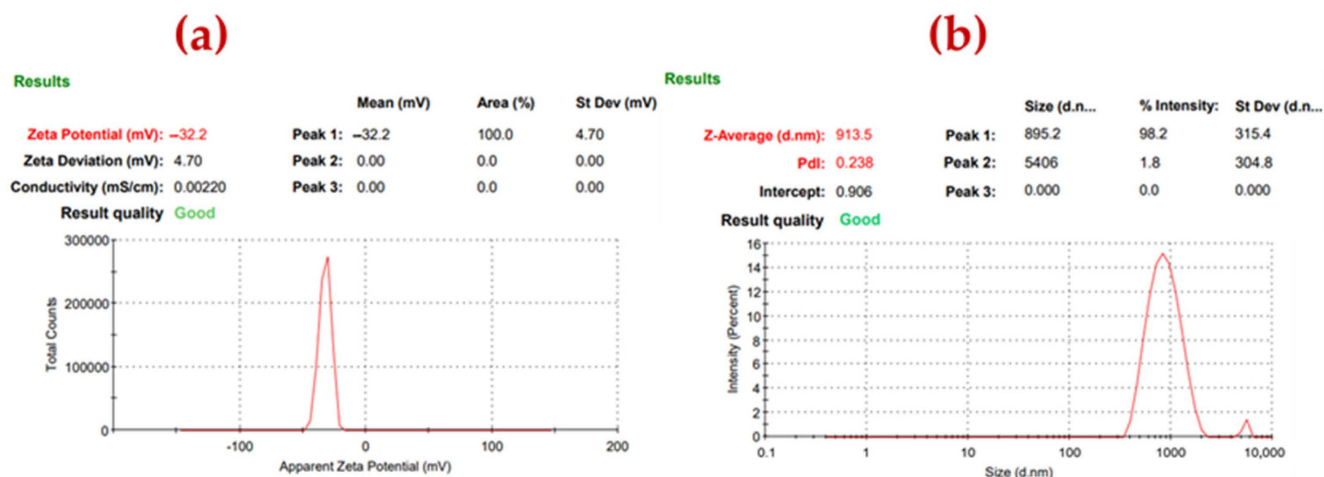


Figure 1. (a) Zeta potential and (b) DLS of CZTSe ink.

3.2. Grazing-Incidence X-ray Diffraction (GI-XRD) Analysis

The XRD diffraction patterns of the as-synthesized CZTSe nanocrystals (Se0, Se1, Se2, Se3, Se0-Na, Se1_Na, Se2_Na, and Se3_Na) are depicted in Figure 2a (without thin sodium layers) and Figure 2b (with thin sodium layers). Sharp XRD diffraction peaks are observed at approximately $2\theta = 27.19^\circ$, 45.25° , and 53.49° , corresponding to d-spacings of approximately 3.276 Å, 2.002 Å, and 1.711 Å, which are attributed to the (112), (204), and (312) planes of the CZTSe kesterite crystal structure (JCPDS card no. 00-052-0868), respectively. Various weak peaks at $2\theta = 17.34^\circ$, 21.98° , 31.75° , 65.94° , and 72.65° , corresponding to the (101), (110), (008), and (332) planes of the annealed CZTSe samples, respectively, were also observed. In addition to the characteristic peaks of the CZTSe absorber, the primary XRD peak of Mo was detected at $2\theta = 40.53^\circ$ (110) as an internal standard, indicating a well-aligned sample height. All the annealed CZTSe samples exhibited polycrystallinity. No characteristic diffraction peaks of secondary phases were found in any of the prepared CZTSe samples with or without sodium. This confirms the formation of a single-phase for all synthesized CZTSe samples.

Structural properties, such as crystallite size, dislocation density, strain, and lattice constants, of the CZTSe samples, were determined using the XRD diffraction pattern as described in our previous study [23]. The data are summarized in Table S1. The determined lattice constants ($a = b = \sim 5.47$ Å and $c = \sim 11.34$ Å) correspond well with the standard lattice constant values of the kesterite CZTSe material ($a = b = 5.69$ Å and $c = 11.33$ Å) (JCPDS card no. 00-052-0868). Tetragonal distortion ($c/2a$ ratio of 1) was observed in all CZTSe samples. These results correspond well with the literature values and further confirm the kesterite structure [14,27]. Using the Debye–Scherrer formula, the crystallite size was estimated to be in the range of 9–45 nm, whereas the average crystallite size obtained using the Williamson–Hall method was approximately 7–50 nm. Smaller crystallite sizes along with higher dislocation densities and strains were observed for the as-synthesized CZTSe as well as Se0 (before annealing). A decrease in the crystallite size and an increase in the

strain and dislocation density with increasing temperature were observed, indicating poor crystallinity (Table S1, ESI). The strain of all CZTSe samples showed a negative slope, which suggests lattice compression toward the *c*-axis (Table S1) [23,28]. The relative intensity ratios of $I_{(112)}/I_{(204)}$ and $I_{(112)}/I_{(312)}$ for Se1 and Se1_Na were observed to be higher than the standard values [$I_{(112)}/I_{(204)} = 2.63$, and $I_{(112)}/I_{(312)} = 5.0$] (Table S2). The relative intensity ratios for the other prepared samples possessed either moderate (Se0, Se2, and Se0_Na) or lower (Se3 and Se3_Na) values compared with those of the standard. A higher intensity ratio indicates that [112] is the preferred orientation for the sample annealed at a lower temperature. This is probably owing to the growth of the MoSe₂ layer, which mainly affects the texturization of the CZTSe material [29,30].

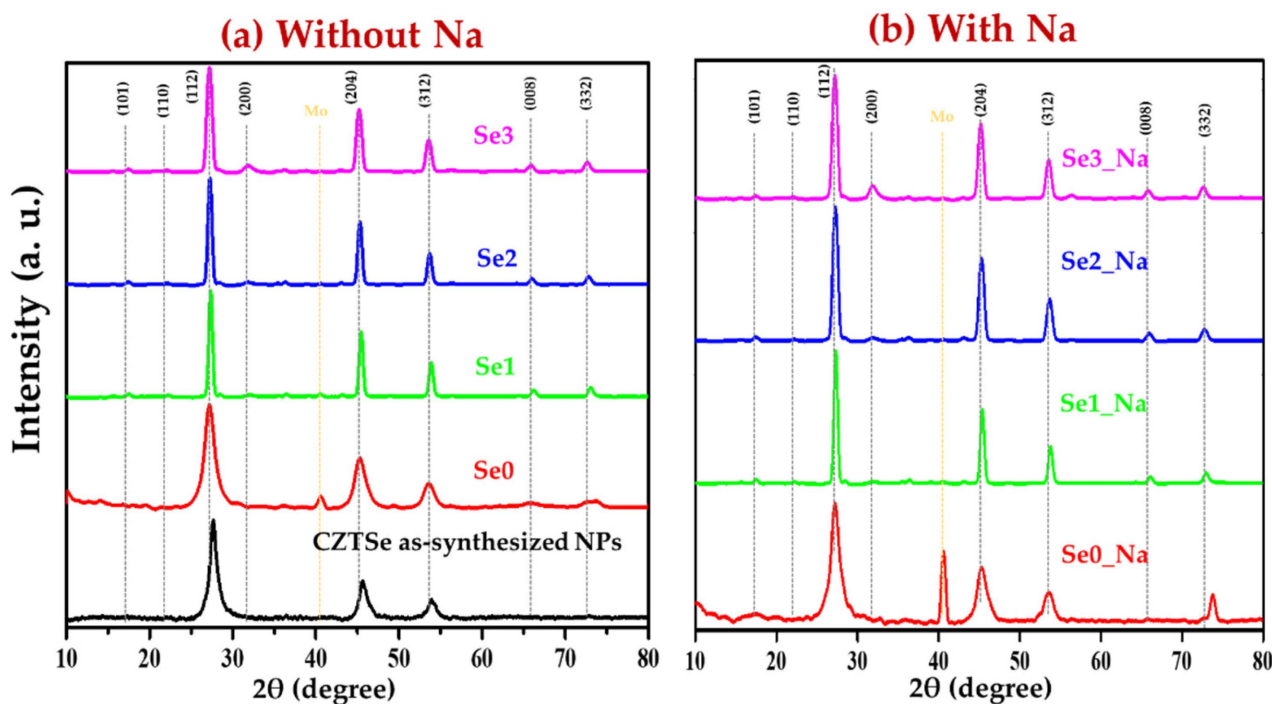


Figure 2. XRD pattern of CZTSe thin films (a) without and (b) with sodium layer.

Notably, the CZTSe XRD diffraction patterns overlap with those of Cu₂Se, ZnSe, and Cu₂SnSe₃. Consequently, the phase purity of CZTSe cannot be confirmed using XRD alone. Raman spectroscopy was, therefore, used to obtain further insights into the phase of the fabricated material.

3.3. Raman Analysis

Raman scattering technique was used to confirm the phase purity of all the prepared CZTSe samples, as shown in Figure 3a–e. Peaks were identified at Raman shifts of 187 and 234 cm⁻¹ for the as-synthesized CZTSe and Se0 samples, respectively (Figure 3a,b). The intense vibrational bands for the annealed samples (Se1, Se2, and Se3) at different temperatures were observed at ~171, ~193, and ~234 cm⁻¹ (Figure 3c–e) [15]. It is currently unknown why two Raman peaks appeared in the samples before annealing, although this has been previously reported [31,32]. The broadening and change in position of the peaks might be due to a change in crystallinity and internal lattice stress [12,33].

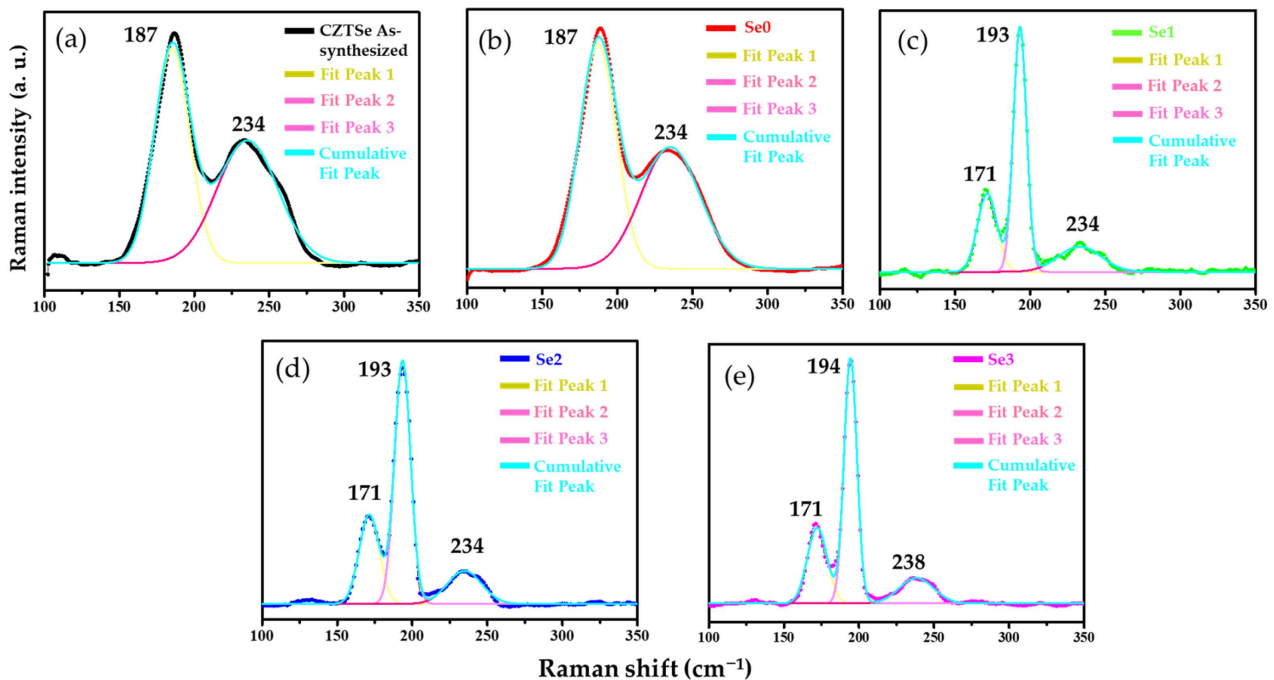


Figure 3. Raman Spectra of CZTSe thin films: (a) As-synthesized CZTSe NP, (b) as-deposited CZTSe thin film (Se0), (c) Se1 (annealed at 500 °C), (d) Se2 (annealed at 520 °C), and (e) Se3 (annealed at 550 °C).

The intense vibrational bands at Raman shifts of 171, 193, and 234 cm^{-1} belong to the CZTSe kesterite phase [15]. The strong bands at 171 and 193 cm^{-1} were attributed to the A1 symmetry mode, which correlates to the vibration of chalcogenide (selenium) atoms within the lattice [14]. The peak at 234 cm^{-1} belongs to the B-symmetry mode. These results are comparable to previously reported CZTSe kesterite Raman peaks [13,15,34]. Raman peaks for other secondary phases, such as binary and ternary phases (e.g., ZnSe and Cu_2SnSe_3), have been reported and are summarized in Table S3. The absence of characteristic peaks of the secondary phases in the Raman spectra for the CZTSe confirmed the formation of a single phase. Raman spectroscopy offers key information to enable the successful characterization of the stannite and kesterite structures of the CZTSe materials. The peaks at 209, 226, 232, and 254 cm^{-1} are suggestive of a stannite structure, contrary to the kesterite structure (at 150–200 (171, 187), 216, 230, and 239 cm^{-1}). The corresponding peaks at 171, 193, and 234 cm^{-1} of the annealed samples closely resembled the kesterite structure. Despite the peaks at 193 and 234 cm^{-1} being close to the peaks at 209 and 232 cm^{-1} of the stannite structure, no peaks were observed at 254 cm^{-1} . These results confirm the formation of single-phase CZTSe kesterite.

3.4. FT-IR Analysis

The FT-IR spectra of the CZTSe samples, PEG-400, and Tween-80 in the range of 400–4000 cm^{-1} are shown in Figure 4a,b. Major FT-IR peaks were observed at approximately 3300, 1700, 1600, and 986 cm^{-1} for samples CZTSe, Se0 and Se1. Additionally, a weak absorption band of metal selenide can be observed in the range of 550–400 cm^{-1} for samples CZTSe, Se0 and Se1 [35,36]. The FT-IR peaks of pure PEG-400 [37] and Tween-80 [38] were observed at approximately 3600, 2900, 1452, 1245, 940, and 800 cm^{-1} (Figure 4a). The band at wavenumber $\sim 2900 \text{ cm}^{-1}$ corresponds to the C–H stretching vibrations of the $-\text{CH}_2$ group, and the peak at 1245 cm^{-1} is attributed to C–O stretching vibrations. The peak at 1452 cm^{-1} corresponds to the C–H bending vibrations of the $-\text{CH}_2$ group. However, asymmetrical bending vibrations of CH_3 were observed. The peak near 900 cm^{-1} corresponds to C–O–C symmetrical stretching. A characteristic peak at 1735 cm^{-1} corre-

sponding to the C=O group was observed in the FT-IR spectrum of Tween-80. The band at approximately 600 cm^{-1} , attributed to the secondary phase (ZnSe), was absent in both Se0 and Se1. The spectra of the Se0 showed absorption bands in regions similar to those of Tween-80 and PEG-400. A possible explanation for this might be that the organic molecules (solvents, binder, and surfactant) used in the ink possess similar FT-IR absorption profiles.

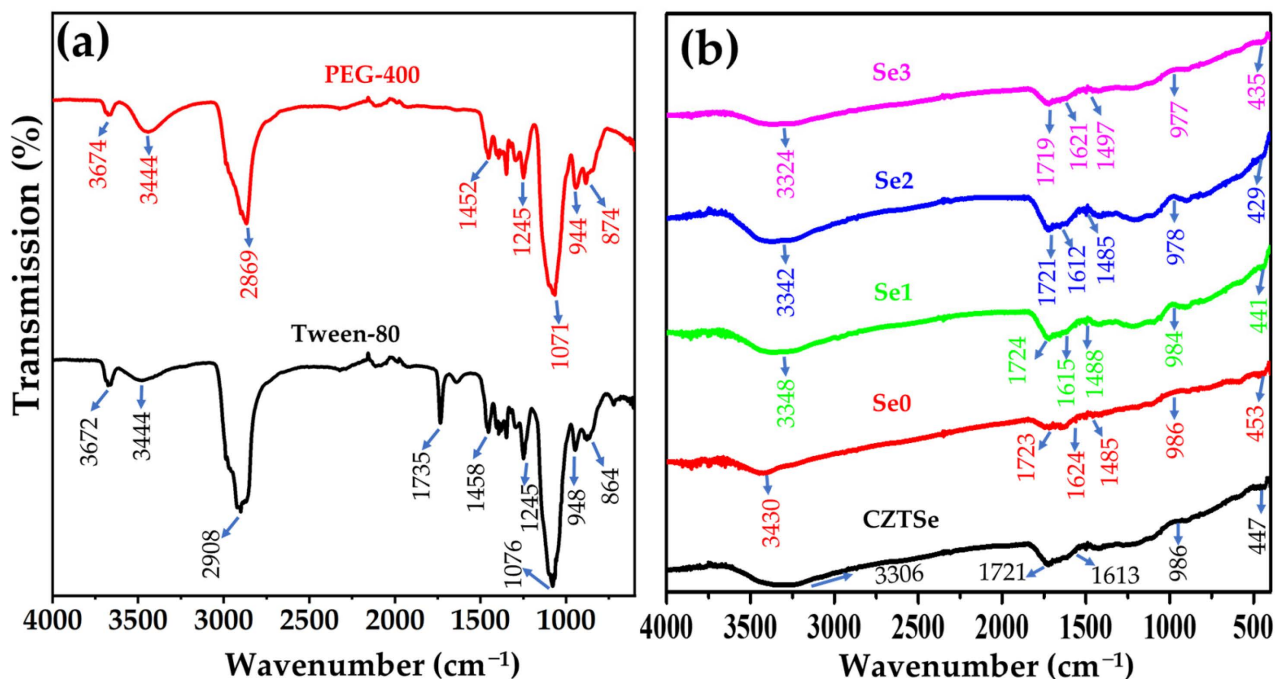


Figure 4. FT-IR spectra of (a) Tween-80 and PEG-400, and (b) CZTSe thin films.

The FT-IR peaks in a similar region were observed for Se2 and Se3 at wave numbers of approximately 3300 , 1700 , 1600 , and 984 cm^{-1} , and these observed peaks are well-match with the unannealed samples. A weak vibrational band of metal selenide was observed in the spectrum at $550\text{--}400\text{ cm}^{-1}$ in the as-synthesized Se2 and Se3 samples [35,36]. However, characteristic peaks $\sim 600\text{ cm}^{-1}$ for ZnSe were not observed, further confirming the formation of single-phase CZTSe [39]. The peak at $\sim 3400\text{ cm}^{-1}$ is attributed to the chalcogen-rich (selenium-rich) composition. The bands at approximately $1600\text{--}900\text{ cm}^{-1}$ belong to the bending and stretching vibrational frequencies of oxygen. These bands arise from hygroscopic materials and surface-adsorbed moisture; that is, H_2O and CO_2 molecules, contributing O-H and C-O-associated peaks in the FT-IR spectrum [39]. FT-IR analysis also confirms the presence of a pure phase in all prepared CZTSe samples.

3.5. FE-SEM and EDS Analyses

The effects of annealing and sodium incorporation on the surface morphology of the CZTSe samples were investigated using FE-SEM. The morphology and cross-sectional images along with the EDS data of Se0, Se1, Se2, and Se3 without a sodium layer are presented in Figure 5, Figure 6, Figure S2 and Figure S4, respectively. Figures S2 and S3 show FE-SEM images of Se0 and Se0_Na thin films, respectively. The surface images show that the Se0 and Se0_Na thin films consisted of nanoparticles and organic residues (PEG-400 and Tween-80), suggesting that the organic additives used for the effective spin coating of the ink were not completely eliminated during the pre-heating step. The minimum temperature for decomposing these molecules into vaporized phases has been reported to be approximately $250\text{ }^\circ\text{C}$ [40,41]. FE-SEM images of the Se0 and Se0_Na thin films showed several voids with small grain sizes on the surfaces. FE-SEM images of the Se1, Se2, and Se3 thin films are presented in Figure 5, Figure 6 and Figure S4, respectively. During

annealing, the organic molecules can be thermally broken down into smaller components and vaporized at high temperatures (500–550 °C). However, some voids with discontinuous grain growth were observed on the surfaces of the samples prepared using this annealing process. Similar surface properties of thin films prepared using nanoparticle ink have also been observed in previous studies [42].

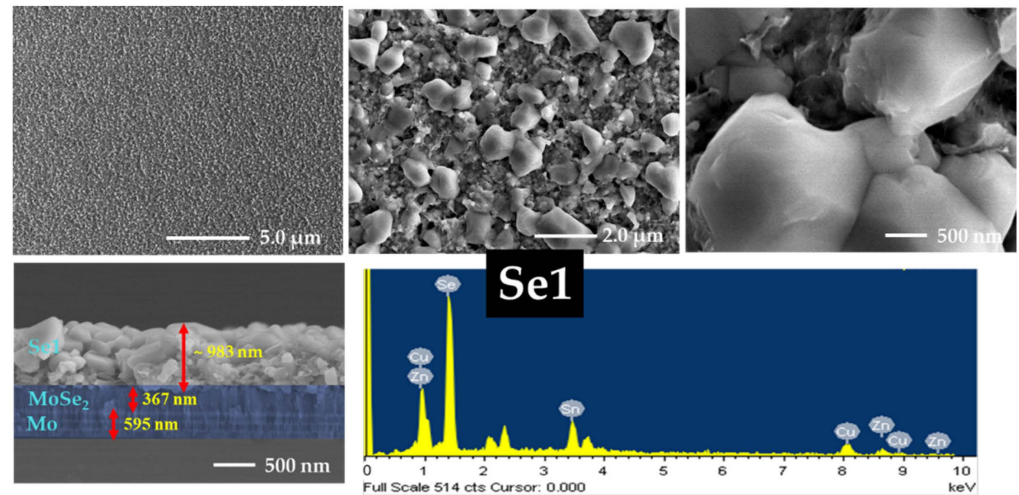


Figure 5. Surface and cross-section images and EDS spectra of Se1 thin film.

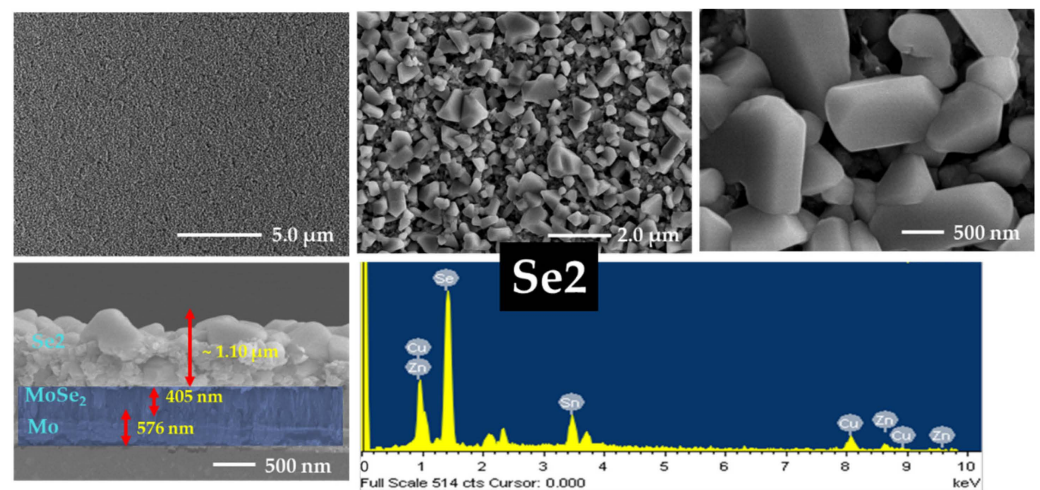


Figure 6. Surface and cross-section images and EDS spectra of Se2 thin film.

The impact of sodium incorporation on the morphology of the Se1_Na, Se2_Na, and Se3_Na thin films was investigated using FE-SEM, as shown in Figure 7, Figure 8 and Figure S5. The surface images show that Se1_Na, Se2_Na, and Se3_Na thin films were non-homogenous, with pinholes and voids, and demonstrated varying grain sizes with discontinuous growth. Although the surface morphology of the thin films is uneven and non-compact, it can aid in evaporating organic materials and reducing carbon residues from the bottom of thin films [43]. The thicknesses of the CZTSe thin films with and without the sodium layer as well as before and after annealing was observed to be in the range of 900 nm to 2.0 μm. Significantly, surface imperfections, such as cracks, voids, and holes, in thin films can increase the series resistance, leading to recombination sites and/or leakage paths in photovoltaic devices.

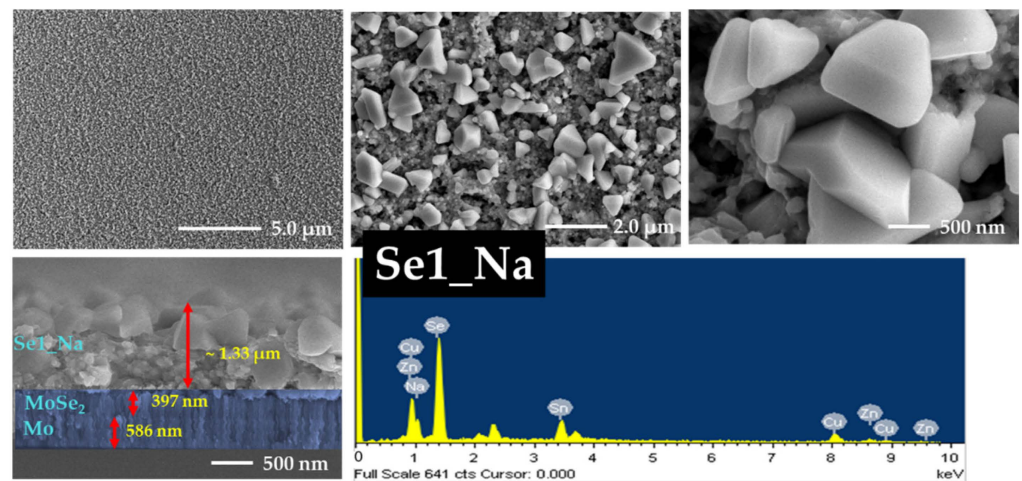


Figure 7. Surface and cross-section images and EDS spectra of Se1_Na thin film with sodium layer.

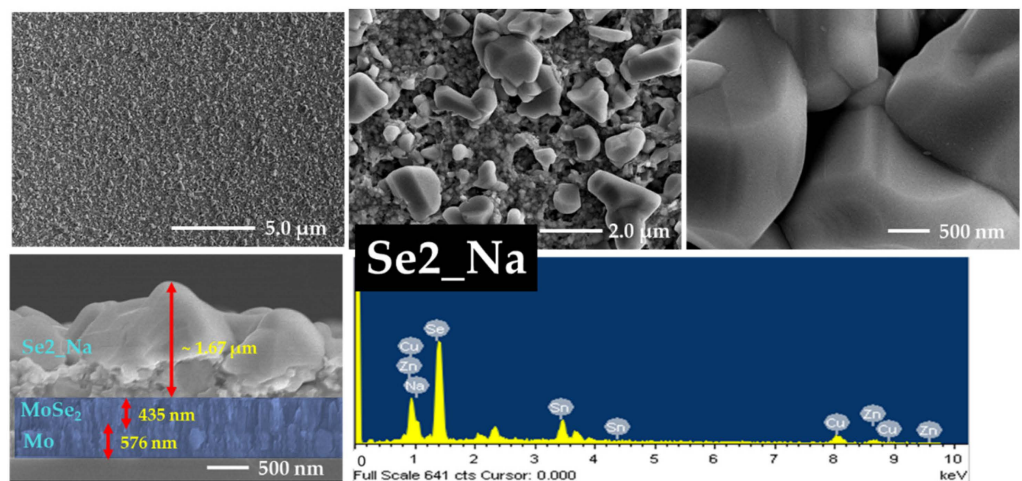


Figure 8. Surface and cross-section images and EDS spectra of Se2_Na thin film with sodium layer.

The formation of a MoSe₂ layer near the interface of the absorber and rare contact layers was observed in the cross-sectional images of all annealed CZTSe samples. Similar to the surface properties of the CZTSe, voids, cracks, and holes were detected on the surface of the thin films during grain growth at different annealing temperatures. These voids, cracks, and holes likely provided channels for the selenium vapors to diffuse. The MoSe₂ layers in Se1, Se2, and Se3 thin films had a thickness of 95, 109, and 178 nm, respectively. In the case of the Se1_Na, Se2_Na, and Se3_Na thin films, the MoSe₂ layers had a thickness of 278, 317, and 377 nm, respectively. The thickness of the MoSe₂ layer was observed to increase with increasing annealing temperature for all CZTSe samples. This may have resulted from the enhanced Se diffusion owing to the poor surface morphology.

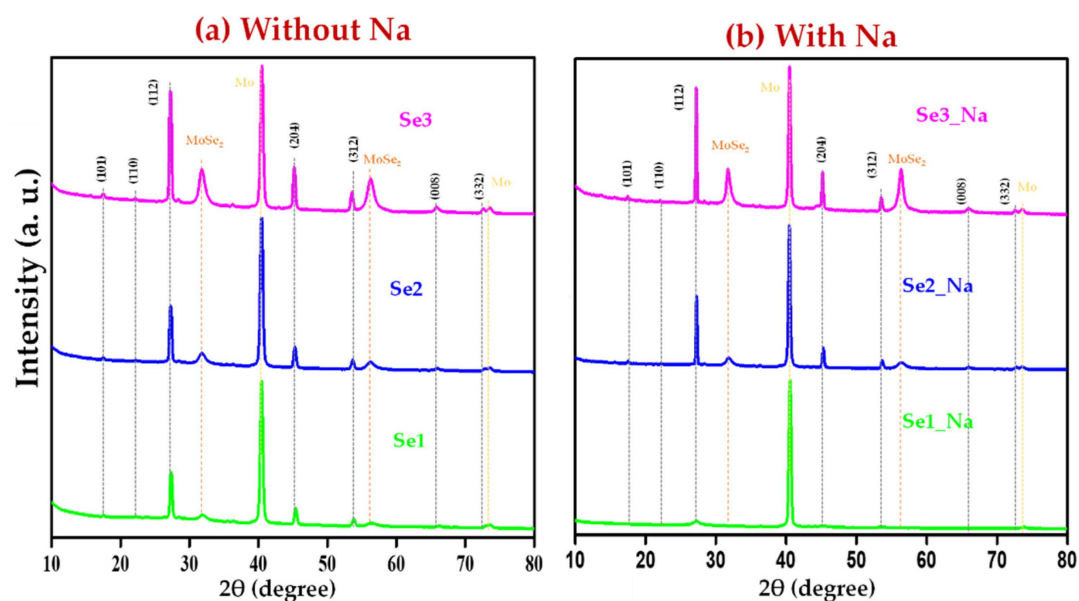
SEM-EDS was used to investigate the chemical composition of the CZTSe; the findings are summarized in Table 1, Tables S4 and S5. The chemical composition profiles of all CZTSe samples were slightly different from each other. A trend with an increasing ratio of Se/(Cu + Zn + Sn) in the CZTSe samples was observed, indicating the substantial incorporation of selenium into the thin films prepared without sodium. The CZTSe thin films prepared with sodium showed an initial decrease, followed by an increase in the Se/(Cu + Zn + Sn) ratio with increasing temperature. The ratios of Cu/(Zn + Sn) and Zn/Sn for all CZTSe samples showed a moderate deviation from the stoichiometric value.

Table 1. Elemental composition of CZTSe without and with sodium layer.

Sl No.	Sample Name	Cu/Zn + Sn	Zn/Sn	Se/(Cu + Zn + Sn)
1	Se0	1.05	1.07	0.86
2	Se1	0.95	1.19	0.85
3	Se2	1.07	1.02	0.89
4	Se3	0.91	1.32	0.92
5	Se0_Na	1.12	0.82	1.03
6	Se1_Na	1.22	0.83	0.89
7	Se2_Na	1.17	0.78	0.92
8	Se3_Na	1.12	1.05	0.98

3.6. Bulk XRD of $\text{Cu}_2\text{ZnSnSe}_4$ Thin Films

To confirm the formation of MoSe_2 at the interface of CZTSe and Mo in the prepared thin films, bulk XRD measurements were conducted. As shown in Figure 9a,b, in addition to the characteristic peaks of the CZTSe thin films, sharp peaks corresponding to Mo were identified at $2\theta \approx 40.56^\circ$ (110) and 73.62° (211), and slightly broad MoSe_2 peaks were observed at $2\theta \approx 31.79^\circ$ (100) and 56.36° (110). [44,45]. The relative intensity of the XRD peaks of MoSe_2 increased with increasing annealing temperature, presumably because of the enhanced selenization of Mo at high temperatures.

**Figure 9.** Bulk XRD patterns of CZTSe thin films (a) without and (b) with sodium layer.

3.7. Optical Properties

The bandgap of the CZTSe samples was determined by plotting $(\alpha hv)^x$ as a function of incident photon energy (hv , eV) (Equation (1)). The linear portion of the spectrum in the high-absorption regime was then extrapolated, yielding the bandgap at the intercept with the photon energy axis [46]:

$$\alpha hv = A(hv - E_g)^x \quad (1)$$

Where α , h , v , and E_g are the absorption coefficient, Planck's constant, light frequency, and optical bandgap (eV), respectively. A and x are both constants. The x value depends on the direct or indirect transition of semiconductor materials. A UV-Vis-NIR spectrophotometer was used to obtain the transmission spectra of the thin films. The absorption coefficient was evaluated using Equation (2) [42]:

$$\alpha = \frac{1}{d} \ln\left(\frac{1}{T}\right) \quad (2)$$

where α is the absorption coefficient, and d and T are the thickness and transmittance of the CZTSe thin film, respectively.

The optical properties of the prepared CZTSe samples were evaluated using transmission spectra in the range of 300–2500 nm, as shown in Figure 10a. The optical properties of semiconductor materials are strongly influenced by surface morphology, explaining the differences in optical properties of CZTSe absorber samples before and after annealing at various temperatures [46]. The optical bandgap values were estimated to be in the range of 0.82–1.02 eV (Figure 10b), which corresponds with the values reported in previous publications [14,15,27,47].

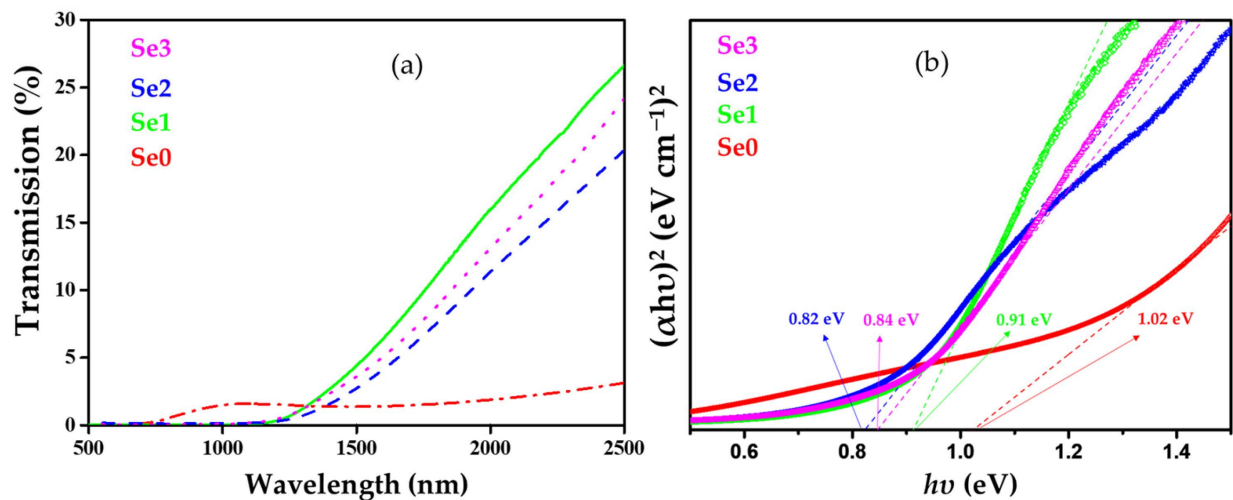


Figure 10. (a) Transmission spectra and (b) bandgap of CZTSe thin films.

3.8. Electrical Properties

The Hall effect using the Van der Pauw method (with a magnetic field intensity of 0.55 T under ambient conditions) was used to investigate the electrical properties. To investigate the impact of annealing and sodium incorporation on the electrical properties, CZTSe thin films were prepared as previously reported [23]. The results are summarized in Table 2.

Table 2. Electrical properties of CZTS thin films with and without Na layer.

Sl. No.	Sample Name	Carrier Conc. (cm ⁻³)	Mobility cm ² /V·s	Resistivity (Ω cm)
1	Se0	2.10 × 10 ¹⁸	1.21	2.47
2	Se1	1.07 × 10 ¹⁸	1.33	4.41
3	Se2	1.05 × 10 ¹⁸	1.54	3.87
4	Se3	1.80 × 10 ¹⁸	1.13	3.06
5	Se0_Na	1.13 × 10 ¹⁸	1.12	4.96
6	Se1_Na	2.04 × 10 ¹⁷	6.71	4.56
7	Se2_Na	6.14 × 10 ¹⁷	1.76	5.77
8	Se3_Na	1.61 × 10 ¹⁹	3.86	0.101

The carrier concentration and mobility of CZTSe samples were measured to be 6.14 × 10¹⁷–1.61 × 10¹⁹ cm⁻³ and 1.13–6.71 cm²/V·s, respectively. These values are similar to published reports (10¹⁵ cm⁻³–10¹⁹ cm⁻³ and 0.1–10 cm²/V·s, respectively) [12,48–50]. Relatively high resistivities (0.1 to 5.8 Ω·cm) were measured, possibly resulting from the uneven grain growth and the porous nature of the thin films. Se3_Na exhibited the highest carrier concentration and lowest resistivity with moderate mobility, although void formation and isolated grain growth were observed in the thin film. All CZTSe samples showed p-type conductivity. Although slight variations in the electrical properties of the CZTSe samples were observed when compared with the reported values of mobility (0.1–10 cm²/V·s),

carrier density (10^{15} – 10^{19} cm^{-3}), and resistivity (10^{-2} – 10 $\Omega\cdot\text{cm}$) [12,27,51,52], however, improvement can be expected by increasing the quality of the films (Table 2).

The results from various analytical techniques, including GI-XRD, Raman, FT-IR spectroscopy, FE-SEM-EDS, UV-Vis-NIR spectrophotometry, and the Van der Pauw measurements, suggest that CZTSe thin films prepared using the nanoparticle ink method can potentially be used as absorber layers to fabricate photovoltaic devices.

3.9. Photovoltaic Analysis: J-V Characteristic

The CZTSe absorber layers with and without sodium were integrated into the photovoltaic device in the traditional configuration of SLG/Mo/CZTSe:Na or CZTSe/CdS/i-ZnO/AZO/Ni-Ag. The photovoltaic performance for all CZTSe photovoltaic devices, where the total active area of each device was 0.40 cm^2 , (measured under 1 sun, AM1.5 irradiation conditions) is presented in Figure 11a and Table 3. Se2 and Se1_Na exhibited the best results among all devices. Se2 had the maximum efficiency ($\eta = 0.16\%$) and short-circuit current density ($J_{\text{sc}} = 1.62$ mA/cm^2), while Se1_Na showed the highest open current-voltage ($V_{\text{oc}} = 335$ mV) and fill factor ($\text{FF} = 44.19\%$). However, the photovoltaic performance of the CZTSe devices (with and without sodium) fabricated in this study was significantly lower compared with that of pure CZTSe devices fabricated using the vacuum-based technique [3,53] and toxic hydrazine-based method [6,54]. The possible reasons for low performance in this study may be as below: (i) the presence of small grains with discontinuous growth and rough surface morphology of the CZTSe samples, (ii) defects, (iii) mismatched energy band alignment at interfaces, (iv) poor crystallinity as increasing the annealing temperature, (v) low or high carrier density, and (vi) formation of MoSe_2 layer at the interface of CZTSe and Mo layers. The high series resistance of thick MoSe_2 can restrict the ability of the Mo electrode to collect photogenerated hole carriers [15,55–57]. This could result in the formation of defective recombination centers, thereby hindering the transport and collection of photogenerated charge carriers and ultimately causing low-performance parameters in the fabricated photovoltaic devices. These findings are being subjected to further investigation in our laboratory to improve the performance of CZTSe-based photovoltaic devices. Figure 11b,c shows cross-sectional images of the photovoltaic devices of Se2 and Se1_Na, respectively.

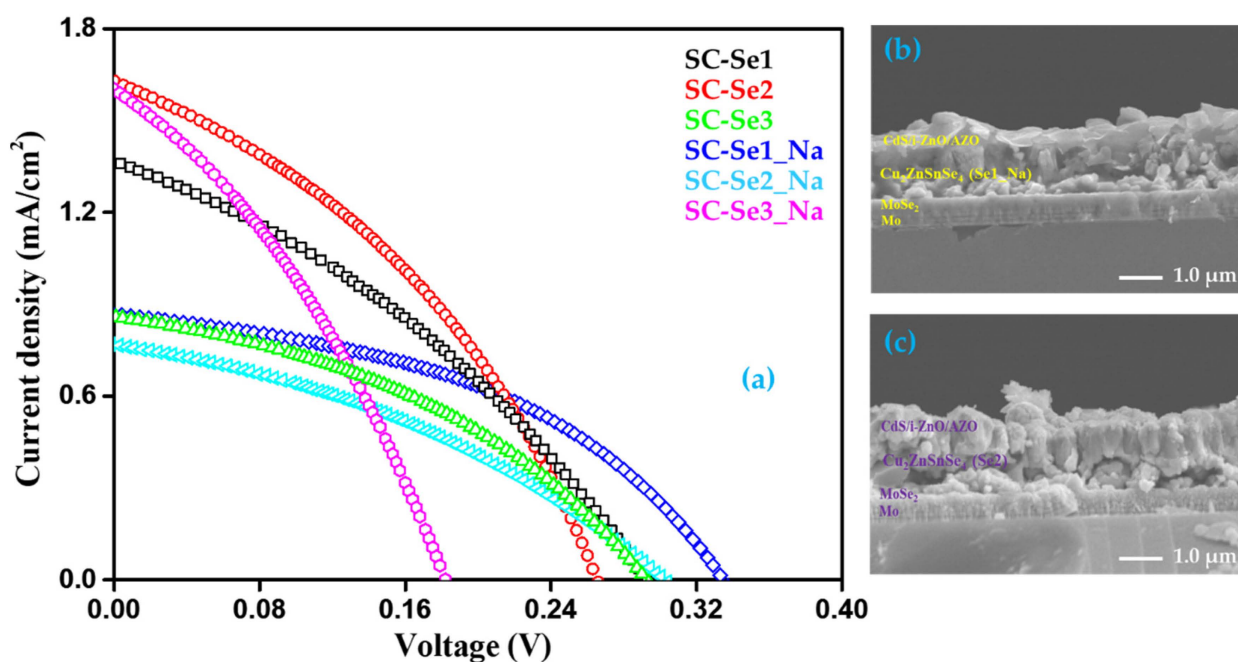


Figure 11. (a) J-V curve of CZTSe photovoltaic device under AM 1.5G illumination, and cross-section image of (b) Se2 and (c) Se1_Na photovoltaic devices.

Table 3. Photovoltaic properties of CZTSe thin films with and without sodium layer.

Sl No.	Sample Name	V _{oc} (mV)	J _{sc} (mA/cm ²)	FF (%)	η (%)
1	SC-Se1	292	1.37	36.56	0.14
2	SC-Se2	266	1.62	37.79	0.16
3	SC-Se3	293	0.85	41.43	0.10
4	SC-Se1_Na	335	0.86	44.19	0.12
5	SC-Se2_Na	300	0.76	41.32	0.10
6	SC-Se3_Na	182	1.60	33.55	0.09

The following strategies have been used in the literature for improving the efficiency of CZTSe cells: (i) Surface treatments or surface passivation: after sintering, the appearance of a high conducting phase, such as Cu_xSe_y on the surface of the CZTSe NPs absorber layer shows a detrimental impact. Therefore, surface treatment, such as KCN etching is necessary to remove those secondary phases. Further, the passivation of CZTSe is necessary. (ii) In order to promote the crystallization, a high-temperature annealing step can be employed, and hence annealing under sulfurization or selenization is essential to increase the grain growth. (iii) The formation of MoSe₂ can be reduced by passivation at the back contact interface. (iv) The deposition and pre-heating conditions can be optimized for the evaporation of the solvent and/or additives since too high drying temperature and speed can cause initial cracks in the deposited films. (v) Carrier doping density can be further optimized. (vi) A Cu-deficient (Cu/(Zn + Sn)~0.8) and Zn-rich (Zn/Sn~1.2) compositions are important for highly efficient photovoltaic devices, and therefore, the elemental composition of CZTSe samples requires further optimization [42,57,58].

4. Conclusions

In this study, single-phase CZTSe thin films were deposited using a simple, reproducible, and cost-effective colloidal ink method, that is, a non-vacuum synthesis technique. The kesterite CZTSe nanoparticles and ink were prepared using a mechanochemical milling process. CZTSe thin films were deposited from the prepared nanoparticle inks via spin-coating using inexpensive and innocuous azeotropic solvents (ethanol and MEK) under ambient conditions. The influence of different annealing temperatures (500–550 °C) and sodium incorporation on the photovoltaic performance and material properties, such as surface morphology, chemical composition, phase purity, optical properties, and electrical properties, were evaluated. The outcomes of material analyses support the successful formation of CZTSe in the single phase. The CZTSe thin films possessed small porous grains with discontinuous growth, regardless of the annealing temperature. EDS analysis showed the substantial incorporation of chalcogen (Se) into the absorber films during annealing at different temperatures. All the obtained CZTSe samples showed p-type conductivity with an optical bandgap between 0.82–1.02 eV. The efficiencies of the photovoltaic device fabricated from Se2 and Se1_Na were 0.16% and 0.12%, respectively. This simple and effective fabrication approach provides a low-cost and controlled method to produce CZTSe samples without the use of hazardous and toxic gases, dangerous solvents, or complicated vacuum equipment.

Supplementary Materials: The following supporting information can be downloaded from: <https://www.mdpi.com/article/10.3390/nano12091503/s1>, Preparation of CZTSe nanopowder, ink, and sodium solution; CZTSe thin-film coating, annealing, and photovoltaic device fabrication; Figure S1: Green synthesis of CZTSe nanoparticle and ink formation via wet ball milling method; Characterization; Table S1: Structural parameter: crystalline (D), strain (ε), dislocation density (δ), and lattice constant (a = b and c) of the CZTSe thin film annealed at different temperatures; Table S2: Relative intensity ratio of CZTSe (112), (204) and (312) plane; Table S3: Raman scattering band position of CZTSe and other secondary phases; Figure S2: Surface and cross-section images and EDS spectra of the Se0 thin film; Figure S3: Surface and cross-section images and EDS spectra of the Se0_Na thin film with the sodium layer; Figure S4: Surface and cross-section images and EDS spectra of the Se3 thin film; Figure S5: Surface and cross-section images and EDS spectra of the Se3_Na thin

film with the sodium layer; Table S4: Elemental composition of CZTSe without the sodium layer; Table S5: Elemental composition of CZTSe with the sodium layer. References [59–62] are cited in the Supplementary Materials.

Author Contributions: Conceptualization, M.S.; investigation, M.S. and V.R.M.R.; data curation, M.S. and V.R.M.R.; analysis and data processing, M.S. and V.R.M.R.; writing—original draft preparation, M.S., V.R.M.R. and B.P.; writing—review and editing, V.R.M.R., W.K.K., C.P. and P.S.; supervision, W.K.K., C.P. and P.S.; funding acquisition, W.K.K., P.S. and C.P. All authors have read and agreed to the published version of the manuscript.

Funding: P.S. (author) acknowledges the IITB-ISRO space technology cell at IIT Bombay for funding this research (project code: 15ISROC002). This research was supported by Priority Research Center Program through the National Research Foundation of Korea (NRF) funded by the Ministry of Education (grant number 2014R1A6A1031189). C.P. acknowledges a KENTECH Research Grant (KRG2021-01-008).

Institutional Review Board Statement: Not applicable.

Informed Consent Statement: Not applicable.

Data Availability Statement: Not applicable.

Acknowledgments: The authors also acknowledge that the e-beam evaporator, DC/RF sputtering system, and Hall Measurements at Yeungnam University, Regional Innovation Center (RIC) for Solar Cell/Module, were employed for solar cell fabrication and characterization.

Conflicts of Interest: The authors declare no conflict of interest.

References

1. Wibowo, R.A. Powder-to-film approach for fabricating critical raw material-free kesterite $\text{Cu}_2\text{ZnSn}(\text{S,Se})_4$ thin film photovoltaic: A review. *Sol. Energy* **2018**, *176*, 157–169. [[CrossRef](#)]
2. Luckert, F.; Hamilton, D.I.; Yakushev, M.V.; Beattie, N.S.; Zoppi, G.; Moynihan, M.; Forbes, I.; Karotki, A.V.; Mudryi, A.V.; Grossberg, M.; et al. Optical properties of high quality $\text{Cu}_2\text{ZnSnSe}_4$ thin films. *Appl. Phys. Lett.* **2011**, *99*, 062104. [[CrossRef](#)]
3. Lee, Y.S.; Gershon, T.; Gunawan, O.; Todorov, T.K.; Gokmen, T.; Virgus, Y.; Guha, S. $\text{Cu}_2\text{ZnSnSe}_4$ thin-film solar cells by thermal co-evaporation with 11.6% efficiency and improved minority carrier diffusion length. *Adv. Energy Mater.* **2015**, *5*, 1401372. [[CrossRef](#)]
4. Li, X.; Zhuang, D.; Zhang, N.; Zhao, M.; Yu, X.; Liu, P.; Wei, Y.; Ren, G. Achieving 11.95% efficient $\text{Cu}_2\text{ZnSnSe}_4$ solar cells fabricated by sputtering a Cu–Zn–Sn–Se quaternary compound target with a selenization process. *J. Mater. Chem. A* **2019**, *7*, 9948–9957. [[CrossRef](#)]
5. Brammertz, G.; Buffière, M.; Oueslati, S.; ElAnzeery, H.; Ben Messaoud, K.; Sahayaraj, S.; Köble, C.; Meuris, M.; Poortmans, J. Characterization of defects in 9.7% efficient $\text{Cu}_2\text{ZnSnSe}_4$ -CdS-ZnO solar cells. *Appl. Phys. Lett.* **2013**, *103*, 163904. [[CrossRef](#)]
6. Bag, S.; Gunawan, O.; Gokmen, T.; Zhu, Y.; Todorov, T.K.; Mitzi, D.B. Low band gap liquid-processed CZTSe solar cell with 10.1% efficiency. *Energy Environ. Sci.* **2012**, *5*, 7060–7065. [[CrossRef](#)]
7. Jeon, J.O.; Lee, K.D.; Seul Oh, L.; Seo, S.W.; Lee, D.K.; Kim, H.; Jeong, J.H.; Ko, M.J.; Kim, B.; Son, H.J. Highly efficient copper–zinc–tin–selenide (CZTSe) solar cells by electrodeposition. *ChemSusChem* **2014**, *7*, 1073–1077. [[CrossRef](#)]
8. Tiwari, K.J.; Ren, M.-Q.; Vajandar, S.K.; Osipowicz, T.; Subrahmanyam, A.; Malar, P. Mechanochemical bulk synthesis and e-beam growth of thin films of Sb_2Se_3 photovoltaic absorber. *Sol. Energy* **2018**, *160*, 56–63. [[CrossRef](#)]
9. Tiwari, K.J.; Kumar, D.P.; Mallik, R.C.; Malar, P. Ball mill synthesis of bulk quaternary $\text{Cu}_2\text{ZnSnSe}_4$ and thermoelectric studies. *J. Electron. Mater.* **2017**, *46*, 30–39. [[CrossRef](#)]
10. Rohini, M.; Reyes, P.; Velumani, S.; Latha, M.; Becerril-Juarez, I.; Asomoza, R. Parametric optimization of mechanochemical process for synthesis of $\text{Cu}(\text{In, Ga})_{0.5}\text{Se}_2$ nanoparticles. *Mater. Sci. Semicond. Process.* **2015**, *37*, 151–158. [[CrossRef](#)]
11. Goyal, D.; Goyal, C.; Ikeda, H.; Malar, P. Role of growth temperature in photovoltaic absorber CuSbSe_2 deposition through e-beam evaporation. *Mater. Sci. Semicond. Process.* **2020**, *108*, 104874. [[CrossRef](#)]
12. Shyju, T.; Anandhi, S.; Suriakarthick, R.; Gopalakrishnan, R.; Kuppusami, P. Mechanochemical synthesis, deposition and characterization of CZTS and CZTSe materials for solar cell applications. *J. Solid State Chem.* **2015**, *227*, 165–177. [[CrossRef](#)]
13. Tiwari, K.J.; Mallik, R.C.; Malar, P. Raman studies of Ball mill synthesized bulk $\text{Cu}_2\text{ZnSnSe}_4$. In *AIP Conference Proceedings*; AIP Publishing LLC: Bhuvaneshwar, Odisha, India, 2017; Volume 1832, p. 060019.
14. Goyal, D.; Malar, P. Dry mill route for synthesis of single phase bulk and e-beam growth of thin films of $\text{Cu}_2\text{ZnSnSe}_4$ for photovoltaic applications. *J. Alloy. Compd.* **2020**, *846*, 156464. [[CrossRef](#)]
15. Liu, Y.; Xu, X.; Liu, K.; Liu, H. Synthesis of $\text{Cu}_2\text{ZnSnSe}_4$ thin-film solar cells from nanoparticles by a non-vacuum mechanical ball milling and rapid thermal processing. *Micro Nano Lett.* **2020**, *15*, 887–891. [[CrossRef](#)]

16. Tampo, H.; Kim, S.; Nagai, T.; Shibata, H. Sodium incorporation effect on morphological and photovoltaic properties for $\text{Cu}_2\text{ZnSnSe}_4$ solar cells. *Jpn. J. Appl. Phys.* **2020**, *59*, SCCD06. [[CrossRef](#)]
17. Kim, J.; Kim, G.Y.; Nguyen, T.T.T.; Yoon, S.; Kim, Y.K.; Lee, S.Y.; Kim, M.; Cho, D.H.; Chung, Y.D.; Lee, J.H.; et al. Sodium-assisted passivation of grain boundaries and defects in $\text{Cu}_2\text{ZnSnSe}_4$ thin films. *Phys. Chem. Chem. Phys.* **2020**, *22*, 7597–7605. [[CrossRef](#)]
18. Rehan, M.; Cho, A.; Amare, A.M.; Kim, K.; Yun, J.H.; Cho, J.S.; Park, J.H.; Gwak, J.; Shin, D. Defect passivation in $\text{Cu}_2\text{ZnSnSe}_4$ thin-film solar cells by novel sodium doping. *Sol. Energy Mater. Sol. Cells* **2021**, *228*, 111138. [[CrossRef](#)]
19. Jackson, P.; Wuerz, R.; Hariskos, D.; Lotter, E.; Witte, W.; Powalla, M. Effects of heavy alkali elements in Cu (In, Ga) Se_2 solar cells with efficiencies up to 22.6%. *Phys. Status Solidi Rapid Res. Lett.* **2016**, *10*, 583–586. [[CrossRef](#)]
20. Lin, S.; Liu, W.; Zhang, Y.; Cheng, S.; Fan, Y.; Zhou, Z.; He, Q.; Zhang, Y.; Sun, Y. Adjustment of alkali element incorporations in Cu (In, Ga) Se_2 thin films with wet chemistry Mo oxide as a hosting reservoir. *Sol. Energy Mater. Sol. Cells* **2018**, *174*, 16–24. [[CrossRef](#)]
21. Yoon, J.H.; Kim, J.H.; Kim, W.M.; Park, J.K.; Baik, Y.J.; Seong, T.Y.; Jeong, J.h. Electrical properties of CIGS/Mo junctions as a function of MoSe_2 orientation and Na doping. *Prog. Photovolt. Res. Appl.* **2014**, *22*, 90–96. [[CrossRef](#)]
22. Hsu, C.H.; Su, Y.S.; Wei, S.Y.; Chen, C.H.; Ho, W.H.; Chang, C.; Wu, Y.H.; Lin, C.J.; Lai, C.H. Na-induced efficiency boost for Se-deficient Cu (In, Ga) Se_2 solar cells. *Prog. Photovolt.: Res. Appl.* **2015**, *23*, 1621–1629. [[CrossRef](#)]
23. Sahu, M.; Reddy, V.R.M.; Kim, B.; Patro, B.; Park, C.; Kim, W.K.; Sharma, P. Fabrication of $\text{Cu}_2\text{ZnSnS}_4$ Light Absorber Using a Cost-Effective Mechanochemical Method for Photovoltaic Applications. *Materials* **2022**, *15*, 1708. [[CrossRef](#)] [[PubMed](#)]
24. Kadlag, K.P.; Rao, M.J.; Nag, A. Ligand-free, colloidal, and luminescent metal sulfide nanocrystals. *J. Phys. Chem. Lett.* **2013**, *4*, 1676–1681. [[CrossRef](#)]
25. Huang, T.J.; Yin, X.; Tang, C.; Qi, G.; Gong, H. A low-cost, ligand exchange-free strategy to synthesize large-grained $\text{Cu}_2\text{ZnSnS}_4$ thin-films without a fine-grain underlayer from nanocrystals. *J. Mater. Chem. A* **2015**, *3*, 17788–17796. [[CrossRef](#)]
26. Nag, A.; Kovalenko, M.V.; Lee, J.-S.; Liu, W.; Spokoyny, B.; Talapin, D.V. Metal-free inorganic ligands for colloidal nanocrystals: S^{2-} , HS^- , Se^{2-} , HSe^- , Te^{2-} , HTe^- , TeS_3^{2-} , OH^- , and NH_2^- as surface ligands. *J. Am. Chem. Soc.* **2011**, *133*, 10612–10620. [[CrossRef](#)] [[PubMed](#)]
27. Prajapat, R.; Sharma, Y. Morphological characterization and microstructural study of $\text{Cu}_2\text{ZnSnSe}_4$ thin films with compositional variation. *Mater. Res. Express* **2019**, *6*, 116459. [[CrossRef](#)]
28. Islam, M.; Rahman, K.; Haque, F.; Akhtaruzzaman, M.; Alam, M.; Alothman, Z.; Sopian, K.; Amin, N. Properties of low temperature vacuum annealed CZTS thin films deposited on polymer substrate. *Chalcogenide Lett.* **2014**, *11*, 233–239.
29. Singh, A.K.; Aggarwal, G.; Singh, R.K.; Klein, T.R.; Das, C.; Neergat, M.; Kavaipatti, B.; van Hest, M.F.M. Synthesis of CZTS/Se and Their Solid Solution from Electrodeposited Cu–Sn–Zn Metal Precursor: A Study of S and Se Replacement Reaction. *ACS Appl. Energy Mater* **2018**, *1*, 3351–3358. [[CrossRef](#)]
30. Shin, B.; Zhu, Y.; Bojarczuk, N.A.; Jay Chey, S.; Guha, S. Control of an interfacial MoSe_2 layer in $\text{Cu}_2\text{ZnSnSe}_4$ thin film solar cells: 8.9% power conversion efficiency with a TiN diffusion barrier. *Appl. Phys. Lett.* **2012**, *101*, 053903. [[CrossRef](#)]
31. Pareek, D.; Balasubramaniam, K.; Sharma, P. Synthesis and characterization of bulk $\text{Cu}_2\text{ZnSnX}_4$ (X: S, Se) via thermodynamically supported mechano-chemical process. *Mater. Charact.* **2015**, *103*, 42–49. [[CrossRef](#)]
32. Amiri, N.B.M.; Postnikov, A. Electronic structure and lattice dynamics in kesterite-type $\text{Cu}_2\text{ZnSnSe}_4$ from first-principles calculations. *Phys. Rev. B* **2010**, *82*, 205204. [[CrossRef](#)]
33. Wang, W.; Shen, H.; Wong, L.H.; Su, Z.; Yao, H.; Li, Y. A 4.92% efficiency $\text{Cu}_2\text{ZnSnS}_4$ solar cell from nanoparticle ink and molecular solution. *RSC Adv.* **2016**, *6*, 54049–54053. [[CrossRef](#)]
34. Rehan, M.; Jeon, H.; Cho, Y.; Cho, A.; Kim, K.; Cho, J.-S.; Yun, J.H.; Ahn, S.; Gwak, J.; Shin, D. Fabrication and characterization of $\text{Cu}_2\text{ZnSnSe}_4$ thin-film solar cells using a single-stage Co-evaporation method: Effects of film growth temperatures on device performances. *Energies* **2020**, *13*, 1316. [[CrossRef](#)]
35. Molla, A.; Sahu, M.; Kumar, Y.; Hussain, S. Soft template mediated synthesis of Bi–In–Zn–S and its efficient visible-light-driven decomposition of methylene blue. *RSC Adv.* **2015**, *5*, 41941–41948. [[CrossRef](#)]
36. Molla, A.; Sahu, M.; Hussain, S. Under dark and visible light: Fast degradation of methylene blue in the presence of Ag–In–Ni–S nanocomposites. *J. Mater. Chem. A* **2015**, *3*, 15616–15625. [[CrossRef](#)]
37. Marcos, M.A.; Cabaleiro, D.; Guimarey, M.J.; Comuñas, M.J.; Fedele, L.; Fernández, J.; Lugo, L. PEG 400-based phase change materials nano-enhanced with functionalized graphene nanoplatelets. *Nanomaterials* **2018**, *8*, 16. [[CrossRef](#)]
38. Liu, Y.; Gu, J.; Zhang, J.; Yu, F.; Wang, J.; Nie, N.; Li, W. LiFePO_4 nanoparticles growth with preferential (010) face modulated by Tween-80. *Rsc Adv.* **2015**, *5*, 9745–9751. [[CrossRef](#)]
39. Indubala, E.; Sarveshvaran, S.; Sudha, V.; Mamajiwala, A.Y.; Harinipriya, S. Secondary phases and temperature effect on the synthesis and sulfurization of CZTS. *Sol. Energy* **2018**, *173*, 215–224. [[CrossRef](#)]
40. Kishore, R.S.; Pappenberger, A.; Dauphin, I.B.; Ross, A.; Buergi, B.; Staempfli, A.; Mahler, H.-C. Degradation of polysorbates 20 and 80: Studies on thermal autoxidation and hydrolysis. *J. Pharm. Sci.* **2011**, *100*, 721–731. [[CrossRef](#)]
41. Pramono, E.; Utomo, S.; Wulandari, V.; Clegg, F. The effect of polyethylene glycol Mw 400 and 600 on stability of Shellac Waxfree. *In J. Phys. Conf. Ser. IOP Publ.* **2016**, *7*, 012054.
42. Tang, D.; Wang, Q.; Liu, F.; Zhao, L.; Han, Z.; Sun, K.; Lai, Y.; Li, J.; Liu, Y. An alternative route towards low-cost $\text{Cu}_2\text{ZnSnS}_4$ thin film solar cells. *Surf. Coat. Technol.* **2013**, *232*, 53–59. [[CrossRef](#)]

43. Chen, J.; Wang, F.; Yang, B.; Peng, X.; Chen, Q.; Zou, J.; Dou, X. Fabrication of $\text{Cu}_2\text{ZnSnS}_4$ thin films based on facile nanocrystals-printing approach with rapid thermal annealing (RTA) process. *Coatings* **2019**, *9*, 130. [[CrossRef](#)]
44. Kaupmees, L.; Altosaar, M.; Volobujeva, O.; Raadik, T.; Grossberg, M.; Danilson, M.; Mellikov, E.; Barvinschi, P. Isothermal and two-temperature zone selenization of Mo layers. *Adv. Mater. Sci. Eng.* **2012**, *2012*, 345762. [[CrossRef](#)]
45. Li, J.; Chen, G.; Xue, C.; Jin, X.; Liu, W.; Zhu, C. $\text{Cu}_2\text{ZnSnS}_4-x\text{Se}_x$ solar cells fabricated with precursor stacked layer ZnS/Cu/SnS by a CBD method. *Sol. Energy Mater. Sol. Cells* **2015**, *137*, 131–137. [[CrossRef](#)]
46. Amal, M.I.; Kim, K.H. Crystallization of kesterite $\text{Cu}_2\text{ZnSnS}_4$ prepared by the sulfurization of sputtered Cu–Zn–Sn precursors. *Thin Solid Film.* **2013**, *534*, 144–148. [[CrossRef](#)]
47. Jirage, S.; Pagare, P.; Garadkar, K.; Bhuse, V. Structural and morphological studies of chemically deposited nanocrystalline and nano-flower like $\text{Cu}_2\text{ZnSnSe}_4$ thin films. *Mater. Today Proc.* **2021**, *45*, 3950–3954. [[CrossRef](#)]
48. Olgar, M.A.; Başol, B.; Atasoy, Y.; Tomakin, M.; Aygun, G.; Ozyuzer, L.; Bacaksız, E. Effect of heat treating metallic constituents on the properties of $\text{Cu}_2\text{ZnSnSe}_4$ thin films formed by a two-stage process. *Thin Solid Film.* **2017**, *624*, 167–174. [[CrossRef](#)]
49. Ito, K.; Nakazawa, T. Electrical and optical properties of stannite-type quaternary semiconductor thin films. *Jpn. J. Appl. Phys.* **1988**, *27*, 2094. [[CrossRef](#)]
50. Saragih, A.D.; Wubet, W.; Abdullah, H.; Abay, A.K.; Kuo, D.-H. Characterization of Ag-doped $\text{Cu}_2\text{ZnSnSe}_4$ bulks material and their application as thin film semiconductor in solar cells. *Mater. Sci. Eng. B* **2017**, *225*, 45–53. [[CrossRef](#)]
51. Chen, D.; Zhao, Y.; Chen, Y.; Wang, B.; Wang, Y.; Zhou, J.; Liang, Z. Hot-injection synthesis of Cu-doped $\text{Cu}_2\text{ZnSnSe}_4$ nanocrystals to reach thermoelectric zT of 0.70 at 450 C. *ACS Appl. Mater. Interfaces* **2015**, *7*, 24403–24408. [[CrossRef](#)]
52. Khadka, D.B.; Kim, S.; Kim, J. Ge-alloyed CZTSe thin film solar cell using molecular precursor adopting spray pyrolysis approach. *RSC Adv.* **2016**, *6*, 37621–37627. [[CrossRef](#)]
53. Li, J.; Huang, Y.; Huang, J.; Liang, G.; Zhang, Y.; Rey, G.; Guo, F.; Su, Z.; Zhu, H.; Cai, L. Defect Control for 12.5% Efficiency $\text{Cu}_2\text{ZnSnSe}_4$ Kesterite Thin-Film Solar Cells by Engineering of Local Chemical Environment. *Adv. Mater.* **2020**, *32*, 2005268. [[CrossRef](#)] [[PubMed](#)]
54. Bag, S.; Gunawan, O.; Gokmen, T.; Zhu, Y.; Mitzi, D.B. Hydrazine-processed Ge-substituted CZTSe solar cells. *Chem. Mater.* **2012**, *24*, 4588–4593. [[CrossRef](#)]
55. Gu, E.; Yan, C.; Liu, F.; Liu, Y.; Su, Z.; Zhang, K.; Chen, Z.; Li, J.; Liu, Y. $\text{Cu}_2\text{ZnSnS}_4$ thin film solar cells from coated nanocrystals ink. *J. Mater. Sci. Mater.* **2015**, *26*, 1932–1939. [[CrossRef](#)]
56. Agarwal, M.; Patel, P.; Vijayan, O. Electrical studies on (Mo/W) Se_2 single crystals. I. Electrical resistivity. *Phys. Status Solidi* **1983**, *78*, 133–136. [[CrossRef](#)]
57. Sahu, M.; Reddy, V.R.M.; Park, C.; Sharma, P. Review article on the lattice defect and interface loss mechanisms in kesterite materials and their impact on solar cell performance. *Sol. Energy* **2021**, *230*, 13–58. [[CrossRef](#)]
58. Shi, C.; Shi, G.; Chen, Z.; Yang, P.; Yao, M. Deposition of $\text{Cu}_2\text{ZnSnS}_4$ thin films by vacuum thermal evaporation from single quaternary compound source. *Mater. Lett.* **2012**, *73*, 89–91. [[CrossRef](#)]
59. Altosaar, M.; Raudoja, J.; Timmo, K.; Danilson, M.; Grossberg, M.; Krustok, J.; Mellikov, E. $\text{Cu}_2\text{Zn}_{1-x}\text{Cd}_x\text{Sn}(\text{Se}_{1-y}\text{S}_y)_4$ solid solutions as absorber materials for solar cells. *Phys. Status Solidi (A)* **2008**, *205*, 167–170. [[CrossRef](#)]
60. Redinger, A.; Hönes, K.; Fontané, X.; Izquierdo-Roca, V.; Saucedo, E.; Valle, N.; Pérez-Rodríguez, A.; Siebentritt, S. Detection of a ZnSe secondary phase in coevaporated $\text{Cu}_2\text{ZnSnSe}_4$ thin films. *Appl. Phys. Lett.* **2011**, *98*, 101907. [[CrossRef](#)]
61. Kim, Y.; Choi, I.-H. High pressure Raman scattering of a co-evaporated Cu_2SnSe_3 thin film. *Thin Solid Film.* **2018**, *647*, 9–12. [[CrossRef](#)]
62. Chihi, A.; Bessais, B. Synthesis and characterization of Cu_2SnSe_3 thin films by electrodeposition route. *Superlattices Microstruct.* **2016**, *97*, 287–297. [[CrossRef](#)]